*Korean J. Chem. Eng.*, 39(12), 3246-3260 (2022)
DOI: 10.1007/s11814-022-1256-3

pISSN: 0256-1115
eISSN: 1975-7220

# Boiling heat transfer characteristics of bionic flower bud structure microchannels

**Zhibo Tang, Chengchao Wang, Cong Qi†, Yuwei Wang, and Lanqi Chen**

School of Low-carbon Energy and Power Engineering, China University of Mining and Technology, Xuzhou 221116, China
(*Received 26 April 2022 • Revised 8 July 2022 • Accepted 10 August 2022*)

**Abstract**−In order to improve the boiling heat transfer capacity within the microstructure, a superhydrophilic surface model with a bionic flower bud structure was established and the flow-boiling heat transfer characteristics were simulated. The temperature, velocity and vapor phase distribution contours under different working conditions were obtained. The effects of different flower spacings, superheat degrees and surfaces on boiling heat transfer were discussed. The study found that the droplet has more vaporization cores on the superhydrophilic surface, and the bubbles can effectively destroy the velocity and temperature boundary layers, thereby enhancing the boiling heat transfer ability. The heat transfer area under the narrow flower spacing is larger, and the vaporization core is more, which is more conducive to boiling heat transfer. When the superheat degree is 80 K, the superhydrophilic surface with the flower spacing L=0 μm has the strongest heat transfer ability, which is 1.59 times that of the common surface, and the mass transfer rate is increased by 23.5%.

Keywords: Boiling Heat Transfer, Microchannel, Bionic Structure, Superhydrophilic Surface

## INTRODUCTION

Advances in the electronics industry have resulted in existing electronic components becoming smaller and more powerful [1,2]. These electronic components generate a large amount of heat due to large loads during operation, which affects their performance [3,4]. Therefore, thermal management of high-power electronic components is necessary. Traditional air cooling has been difficult to meet the heat dissipation needs of existing high-power equipment. After much basic research, more effective methods have been developed [5-7]. Boiling heat transfer utilizes the latent heat released during the liquid phase change process for heat transfer [8-10], and its heat transfer effect is higher than that of single-phase heat transfer [11-13], proving to be an efficient heat dissipation scheme [14-16]. The mechanism of flow boiling in microchannels is complex, and surface wettability and roughness have important effects on heat transfer. To explore various boiling heat transfer mechanisms, various enhanced heat transfer surfaces [17-20] such as superhydrophilic surfaces [21-23] have been developed.

A large number of scholars have prepared superhydrophilic surfaces by different methods. Kaya et al. [24] prepared the hydrophilic surface by the sol-gel method and found that the contact angle varies between 65° and 4° with the change of the silica content in the spin coating solution, and when the contact angle is less than 15°, the surface has good anti-fog and light transmission properties. Adachi et al. [25] prepared a lightweight polycarbonate-based titania/silica superhydrophilic photocatalytic coating by a sol-gel method. The results showed that light transmittance can reach 85%, anti-fogging ability is improved, and surface haze is reduced from 1.2% to 0.45%. Ma et al. [26] prepared diamond films with different wettability by chemical vapor deposition, and the characterization results showed that the superhydrophilic diamond films have high hardness, high chemical inertness and reusability, and can be used as microcurrent sensors. Mähringer et al. [27] fabricated nanopillar surfaces with metal-organic framework by physical vapor deposition. The results showed that these surfaces show superhydrophilic and underwater superoleophobic properties, and when used to test oil-water separation, the efficiency can reach 99.99%. Sato et al. [28] imitated the microstructure of butterfly wings by a template method, and prepared a superhydrophilic structure color film by regulating the particle concentration and controlling the lifting speed. Deng et al. [29] prepared a superhydrophilic membrane by mixing polyethyleneimine with polyvinylidene fluoride by a phase separation method. The hybrid membrane exhibits excellent performance in oil-water emulsion separation and can be used repeatedly and in long-term operation.

With the development of micro/nano-scale heat transfer, the heat transfer of superhydrophilic surfaces has also received extensive attention, and it is of certain significance to apply it in engineering to solve the problem of heat dissipation. Feng et al. [30] used the lattice-Boltzmann method to study the boiling heat transfer of a hydrophilic-hydrophobic mixed cylindrical surface. The results showed that the existence of the columnar structure can effectively enhance the heat transfer capacity. Liao et al. [31] prepared the superhydrophilic surface of $TiO_2$ coating and compared the surface heat transfer performance under different contact angles. The results showed that the superhydrophilic surface can accelerate heat transfer and its heat flux can reach three times that of common surfaces. Liu et al. [32] studied the effect of different structures of hemispherical surfaces on the boiling heat transfer characteristics, and the results showed that the hydrophilic concave structure could help improve the heat transfer performance. Vontas et al. [33] numerically studied the effect of surface wettability on boiling heat transfer and found that liquid film evaporation is the main heat transfer mechanism

†To whom correspondence should be addressed.
E-mail: qicong@cumt.edu.cn
Copyright by The Korean Institute of Chemical Engineers.

on hydrophilic surfaces. Phan et al. [34] prepared a surface with a contact angle of 20-110° by nano-spin coating, and experimentally studied its nucleate boiling heat transfer ability. They found that the surface with a contact angle of 20° shows the best heat transfer performance. Sia et al. [35] prepared graphene nanosheet superhydrophilic coatings by thermal curing. It was found that the nanocapillary grid structure promotes the rapid penetration of water, induces membrane boiling heat transfer, and inhibits the local drying up during the boiling process. The maximum boiling heat transfer coefficient is increased by 64.9%. Yang et al. [36] prepared metal-organic framework films with hydrophilic properties. By studying the surface boiling heat transfer, it was found that compared with the bare copper mesh, having nanopores in the new film increases the interfacial area, slows the drying of the liquid, the enhancement of wettability increases the surface critical heat flux by 205%, and increases the heat transfer coefficient by 90%. Lim et al. [37] prepared graphene nanosheet films with superhydrophilic properties. It was found that due to the fast water permeability of the surface, nucleate boiling phenomenon is significantly enhanced and water molecules quickly form an ultra-thin water film on the surface of the nanostructure, which promotes the absorption of the latent heat of vaporization. Compared with an uncoated surface, the boiling heat transfer coefficient is increased by 1,178%, and the surface temperature is decreased by 15.5 K. When the coating is applied to the LED equipment, the lifespan is extended by 2.93 times. Ze et al. [38] fabricated a copper-based superhydrophilic microcavity composite nanocone structure. The results showed that the pyramidal structure is an effective nucleation point, the shallow microcavity at the micron scale can avoid excessive thermal resistance, and the ultra-high wettability can improve the critical heat flux. Compared with the smooth copper surface, the maximum heat transfer coefficient is increased by 142%, and the critical heat flux is increased by 64%. Nam et al. [39] prepared a copper-based superhydrophilic surface and studied the formation of single bubbles on the surface. It was found that the diameter of the bubbles generated is 2.5 times smaller than that of the hydrophilic silicon surface, and the growth period is 4 times shorter. Lin et al. [40] simulated the boiling of superhydrophilic and superhydrophobic surfaces and found that the critical heat flux on the surface of the superhydrophilic network structure is increased by 55%, which can effectively delay the occurrence of film boiling. Compared with the superhydrophobic surface, the bubble density and viscosity of the superhydrophilic surface are smaller, and the boiling liquid is easier to reflux. Zhan et al. [41] carried out a numerical simulation of the boiling heat transfer of surfaces with different wettability by the lattice-Boltzmann method, studied the nucleation mechanism of single bubble under the condition of local heat transfer, and extended to multiple bubbles, the boiling curves of non-mixed wettability surfaces were drawn. Ling et al. [42] investigated the boiling of superhydrophilic surfaces in a 2D model by the VOSET method. It was found that when the bubble broke away from surface, the superheated liquid was removed from the surface by the vortex behind the bubble, which could reduce the local overheating phenomenon. Vontas et al. [43] investigated the saturated flow boiling state in microchannels with different wettability at three-dimensional scale. By analyzing the bubble growth process and measuring the interfacial heat transfer coefficient, it was found that the heat transfer performance of hydrophilic and hydrophobic microchannels was improved by 43.9% and 17.8% compared with ordinary surfaces.

In this paper, considering that the superhydrophilic surface is complex and has different structures, a simplified bionic flower bud structure model was constructed, and the flow boiling heat transfer characteristics of the superhydrophilic surface were calculated by the commercial software Fluent. The gas phase distribution, temperature and velocity distribution in boiling heat transfer on different surfaces, different bud spacings and different superheat degrees were specifically studied. The innovations of this paper are as follows: First, a simplified bionic flower bud superhydrophilic model was established. Secondly, the effects of different flower spacing and superheat degrees on flow boiling heat transfer were studied. Finally, the temperature and velocity distributions of the boiling heat transfer between the ordinary surface and the superhydrophilic surface were analyzed, and the boiling heat transfer performance of the two surfaces was compared. Results can provide a certain guiding significance for the application of biomimetic superhydrophilic surfaces to heat pipes for thermal management of electronic components.

## METHODOLOGY

### 1. Physics Model

A superhydrophilic surface at the microscale is simplified to a two-dimensional structure, as shown in Fig. 1. The lower surface is the hot-side, and different superheat conditions are achieved by changing the boundary wall temperature. Both inlets and outlets diameters are 40 μm and the widths are 200 μm. On the superhydrophilic surface, the bud radius $R_b$=5 μm, and the flower spacing L=0, 5, 10 μm. The inlets and outlets are reserved for 40 μm to allow the fluid to develop fully to avoid the inlet effect.

### 2. Numerical Method

Fluent is mainly used for numerical calculation, and the physical model and mesh required for simulation are drawn by Design-

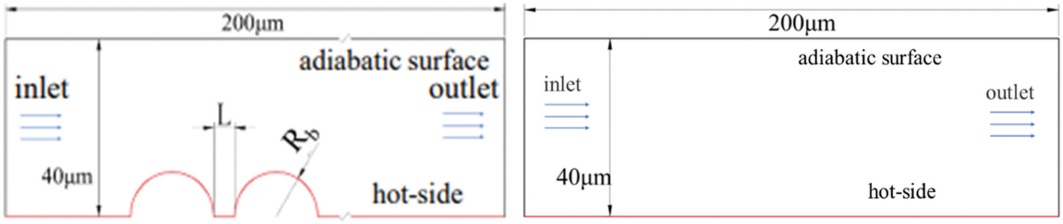



**Fig. 1. Microscopic model of superhydrophilic surface and general surface.**

Modeler (DM) and Mesh integrated in Ansys Workbench. In this paper, the gas-liquid two are incompatible with each other. To obtain good separation results of the phase interface, the model adopts the VOF model.

According to the law of conservation of mass, the continuity equation is shown in Eq. (1)

$$\nabla \cdot \rho U + \frac{\partial \rho}{\partial t} = 0 \tag{1}$$

where $\rho$ is density, u is velocity, and t is time.

In the VOF model, each phase shares a momentum equation whose form is shown in Eq. (2)

$$\frac{\partial}{\partial t}(\rho \vec{u}) + \nabla \cdot (\rho \vec{u}\vec{u}) = \rho \vec{g} - \nabla p + \nabla \cdot [\mu(\nabla \vec{u} + \nabla \vec{u}^{T})] + F_{CSF} \tag{2}$$

where p is pressure, g is gravitational acceleration, and $\mu$ is dynamic viscosity.

The energy equation is shown in Eq. (3):

$$\frac{\partial}{\partial t}(\rho E) + \nabla \cdot (\vec{u}(\rho E + p)) = \nabla \cdot (k \nabla T) + S_E \tag{3}$$

where E is the internal energy, k is the thermal conductivity, T is the temperature of the working medium, and $S_E$ is the energy source term.

Based on the Hertz-Knudsen equation [44], the phase change mass flow F is shown in Eq. (4):

$$F = \beta \sqrt{\frac{M}{2\pi R T_{sat}}} (P^{*} - P_{sat}) \tag{4}$$

where M is the molar mass, R is the gas constant, $T_{sat}$ is the saturation temperature, $P^{*}$ is the gas phase pressure, $P_{sat}$ is the saturation pressure. $\beta$ is the accommodation coefficient, which represents the part of the gas phase molecule adsorbed by the liquid surface and can be taken as 1 under equilibrium condition.

The Clapeyron-Clausius equation [45] relates pressure and temperature at saturation, as shown in Eq. (5):

$$\frac{dP}{dT} = \frac{L_{qr}}{T(1/\rho_v - 1/\rho_l)} \tag{5}$$

where $L_{qr}$ is latent heat.

Integrating Eq. (5) gives Eq. (6):

$$(P^{*} - P_{sat}) = -\frac{L_{qr}}{T_{sat}(1/\rho_v - 1/\rho_l)} (T^{*} - T_{sat}) \tag{6}$$

where $T^{*}$ is the gas phase temperature.

Eq. (7) can be obtained from Eq. (6) and Eq. (4):

$$F = \beta \sqrt{\frac{M}{2\pi R T_{sat}}} L_{qr} \left(\frac{\rho_v \rho_l}{\rho_l - \rho_v}\right) \frac{(T^{*} - T_{sat})}{T_{sat}} \tag{7}$$

The relationship between the interfacial area $A_i$ and the volume fraction of the gas or liquid phase $\alpha_k$ can be defined by Eq. (8):

$$A_i = \frac{6\alpha_k}{d_b} \tag{8}$$

where $d_b$ is the bubble diameter, $\alpha_k$ is the volume fraction of the gas or liquid phase.

The mass source term is obtained from Eq. (9):

$$FA_i = \frac{6}{d_b} \beta \sqrt{\frac{M}{2\pi R T_{sat}}} L_{qr} \left(\frac{\alpha_v \rho_v}{\rho_l - \rho_v}\right) \left[\alpha_l \rho_l \frac{(T^{*} - T_{sat})}{T_{sat}}\right] \tag{9}$$

The evaporative mass transfer rate can be calculated from Eq. (10):

$$\dot{m}_{lv} = \eta_e \alpha_l \rho_l \frac{(T_l - T_{sat})}{T_{sat}} \tag{10}$$

Combining Eq. (9) and Eq. (10), the evaporation coefficient can be calculated by Eq. (11):

$$\eta_e = \frac{6}{d_b} \beta \sqrt{\frac{M}{2\pi R T_{sat}}} L_{qr} \left(\frac{\alpha_v \rho_v}{\rho_l - \rho_v}\right) \tag{11}$$

The mass source term $S_M$ and the energy source term $S_E$ are related by Eq. (12):

$$S_E = S_M * L_{qr} \tag{12}$$

The latent heat $L_{qr}$ is calculated from Eq. (13):

$$L_{qr} = (h_v^s - h_l^s) \tag{13}$$

where $h_v^s$ and $h_l^s$ are the enthalpies of saturation state at saturation temperatures of gas and liquid phases.

## 3. Grid Division

Mesh is used for meshing in this paper, as shown in Fig. 2, which are super-hydrophilic surface meshes with smooth surface and flower spacing L=0, 5, and 10 μm. To capture the surface bubbles and temperature distribution during the evaporation process, the mesh of the hot-side is refined. The number of boundary layer grids is 8, the thickness is 1 μm, and the growth rate is 1.2. To improve the mesh quality, the mesh with smooth surface is divided into structured mesh under the two-dimensional model, and the internal mesh is basically quadrilateral mesh. Due to the existence of bud structure on the superhydrophilic surface, the mesh adopts unstructured division, but the mesh of the hot-side is refined, so the average quality can reach 0.95.

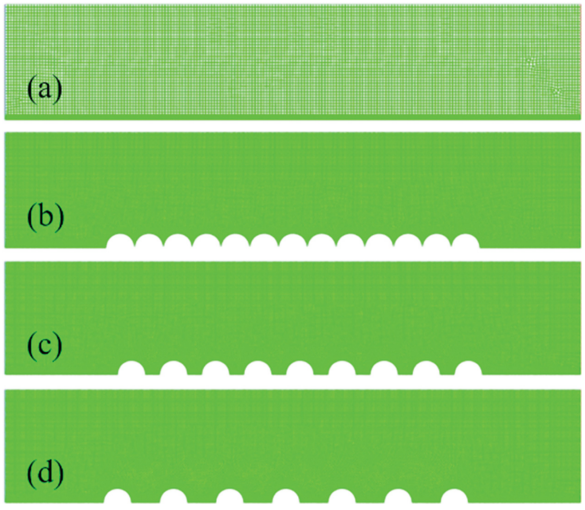



**Fig. 2. Schematic diagram of grid division. (a) common surface; (b) L=0 μm; (c) L=5 μm; (d) L=10 μm.**

**Table 1. Grid independence verification of smooth surface**

| Number of grids | 5,237 | 6,408 | 8,531 | 9,372 | 11,724 |
|---|---|---|---|---|---|
| $T_{out}$ | 393.2298 | 393.2286 | 393.2137 | 393.2077 | 393.2058 |

**Table 2. Grid independence verification of L=0 μm**

| Number of grids | 7,708 | 9,847 | 11,3245 | 12,438 | 13,569 |
|---|---|---|---|---|---|
| $T_{out}$ | 409.0092 | 409.0052 | 408.9968 | 408.9895 | 408.9871 |

**Table 3. Grid independence verification of L=5 μm**

| Number of grids | 7,554 | 9,468 | 11,079 | 12,040 | 12,929 |
|---|---|---|---|---|---|
| $T_{out}$ | 404.1604 | 404.1574 | 404.1496 | 404.1426 | 404.1402 |

**Table 4. Grid independence verification of L=10 μm**

| Number of grids | 7,143 | 8,986 | 10,199 | 11,806 | 12,125 |
|---|---|---|---|---|---|
| $T_{out}$ | 403.1364 | 403.1294 | 403.1211 | 403.1150 | 403.1133 |

## 4. Grid Independence Verification

To ensure the accuracy of the calculation, the established model needs to be verified before the simulation starts. Due to the limitation of computing resources, the lowest grid density can be used to ensure the maximum utilization of computing resources while ensuring that the calculation results are within a very small variation range. To test the relationship between the calculation results and the mesh density, mesh independence verification was carried out. The results are shown in Table 1, Table 2, Table 3 and Table 4. Taking the smooth surface at a superheated degree of 80 K as an example, as the number of meshes increases, the outlet temperature tends to be consistent. Comparing the models with grid numbers of 9,372 and 11,724, the temperature remains basically unchanged. To save computing resources, a model with a grid number of 9,372 was used.

## 5. Model Validation

To further verify the reliability of the model, the simulation results were compared with the data in similar literature [46]. A smooth surface with a superheat of 50 K was selected as the verification model. After the calculation results were stable, the surface heat transfer coefficients were compared. The results are shown in Fig. 3. The error value after stabilization is less than 7%, which proves that the simulation results are acceptable.

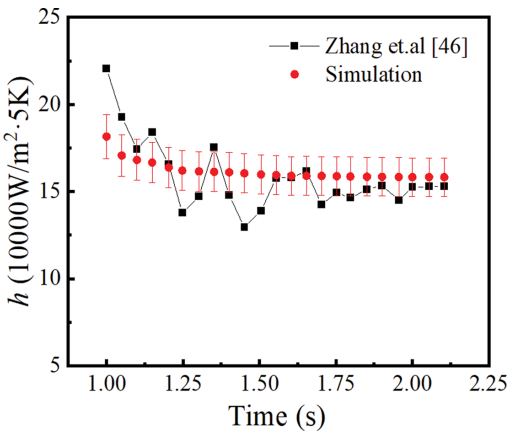



**Fig. 3. Comparison of heat transfer coefficients after stabilization.**

## 6. Calculation Method and Boundary Conditions

In this study, the VOF model was used for the multiphase flow calculation, and the transient calculation was used to monitor the boiling situation in real time. The implicit calculation was used in the volume fraction solution, and the Sharp type was selected in the inner surface model. Water vapor was the main phase, and the secondary phase was liquid water. The surface tension coefficient between the two phases was 0.072. The number of mass transfer model was 1, the evaporative condensation model from water to steam was selected, the default evaporative condensation coefficient was 0.1, and the phase transition temperature was the saturation temperature of 373 K. Considering the existence of heat transfer, the energy equation was chosen. Considering the complexity of the internal flow field, the Realizable model in the k-$\varepsilon$ turbulence model was adopted. To better capture the temperature field near the wall, an enhanced wall treatment and viscous heating settings were used. The other material parameters were kept at default, the molar mass was changed to 18 kg/kmol, the phase change heat transfer was considered, the standard state enthalpy of liquid phase was set to 0, and the standard state enthalpy of gas phase was 40,636,800 J/kg·mol. To save computational cost, the pressure-velocity coupling adopts the SIMPLE algorithm, the volume fraction adopts Compressive, the momentum energy adopts the Second Order Upwind, and the others are default.

To speed up the calculation, the initial inlet liquid temperature was taken as 372 K. The volume fraction of the inlet and outlet liquids was taken as 1. The inlet velocity was taken as 2 m/s. The hot-side of the lower wall was 393, 423, and 453 K respectively, and the upper wall was adiabatic condition. The direction of gravity was the negative direction of the y-axis, taking 9.81 m/s$^2$. To reach equilibrium as soon as possible, the internal temperature was taken as

the saturation temperature during initialization, and the internal liquid volume was 1. To improve the convergence of the transient calculation, a time step was calculated after initialization, the scale was $1\times10^{-7}$ s, and the number of iterations was 500 times, and the calculation results were used as the results of the initialization, and the time step was $5\times10^{-4}$ s. The number of iterations in each time step was reduced to 40.

## RESULTS AND DISCUSSION

### 1. Heat Transfer Properties of Smooth Surfaces

Fig. 4 shows the gas phase distribution at a superheat of 80 K, the red part is steam and the blue part is liquid water. In the initial state, there are about five vaporized cores. Over time, the bubbles grow gradually, and adjacent bubbles merge and eventually break away from the wall. It can be seen from t=1.3-1.5 s, where the bubbles leave, a new bubble core is formed, thus circulating the heat away from the wall. At this superheat, the common surface is still nucleated boiling and no obvious gas film is formed. Compared with Fig. 5, the difference is that the frequency of bubble growth and detachment on the surface is higher, and the bubbles with larger diameter are more, indicating that the boiling state of the surface is more intense under the condition of high superheat.

Fig. 5 shows the temperature distribution at a superheat of 80 K. In the early stage of boiling, the high temperature layer near the hot-side at the bottom is thicker, this part of the liquid absorbs heat rapidly, reaches a saturated state and begins to transition to the gas phase. The overall temperature gradient inside the model is large, but because the specific heat capacity of the liquid is much larger than that of the gas phase, the input heat is limited, and the temperature near the adiabatic surface is difficult to increase. In the early stage of boiling, as shown at t=0.3-0.7 s, a local temperature peak appears in the part where the bubbles grow, indicating that the surface heat enters into the liquid after boiling. Then, as shown at t=1.3 s, as the bubbles merge and separate, a disturbance is caused near the hot-side, which destroys the high temperature layer, so

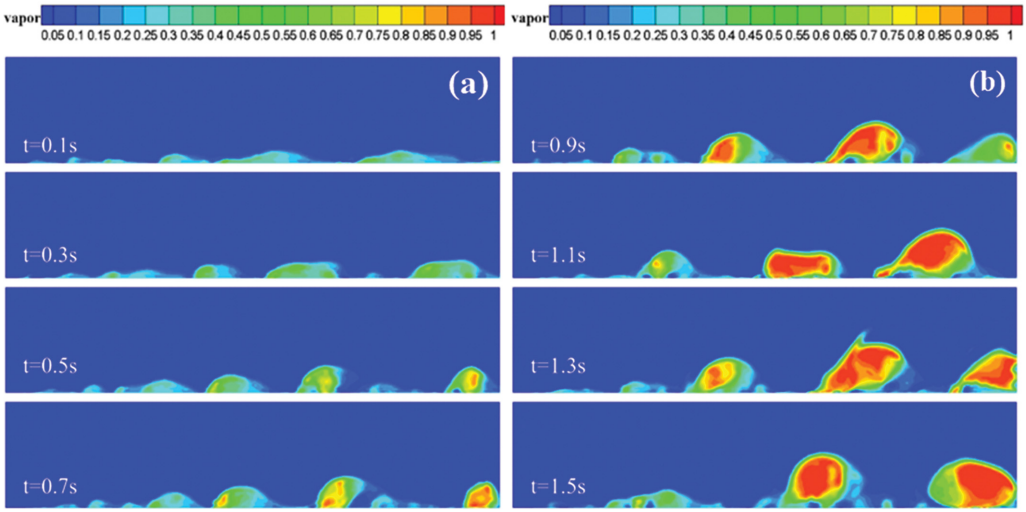



**Fig. 4. Vapor phase distribution at different time with a superheat of 80 K. (a) t=0.1-0.7 s; (b) t=0.9-1.5 s.**

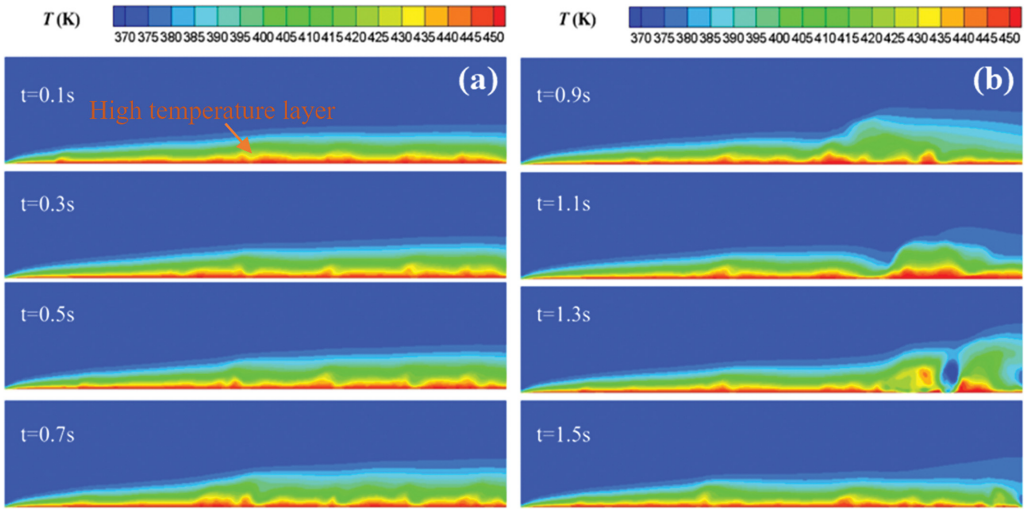



**Fig. 5. Temperature distribution at different time with a superheat of 80 K. (a) t=0.1-0.7 s; (b) t=0.9-1.5 s.**

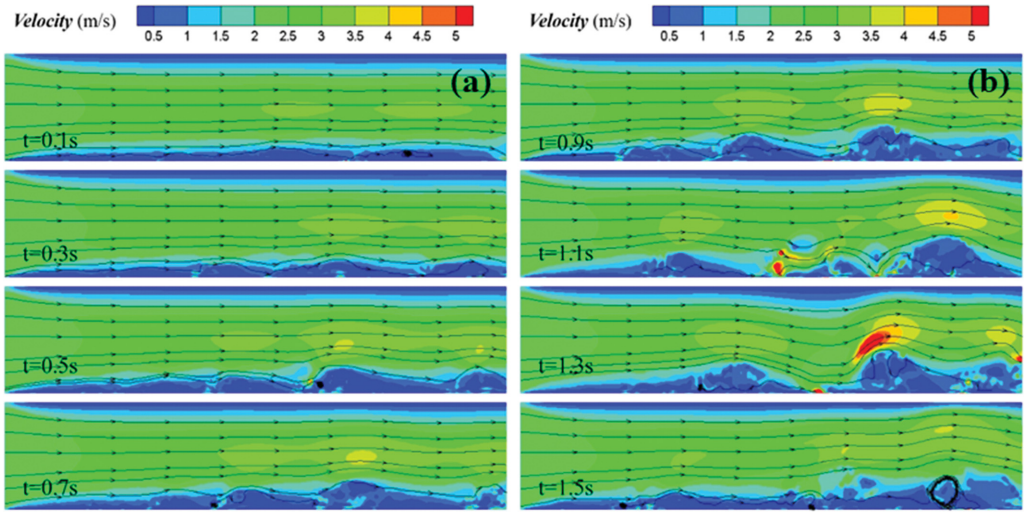



**Fig. 6. Velocity distribution and steam line at different time with a superheat of 80 K. (a) t=0.1-0.7 s; (b) t=0.9-1.5 s.**

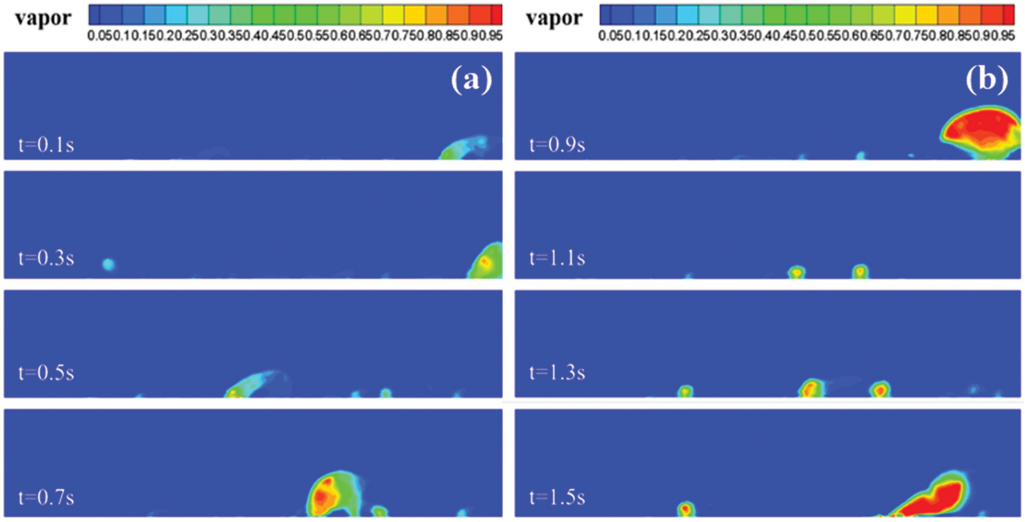



**Fig. 7. Vapor phase distribution at different time with a superheat of 50 K. (a) t=0.1-0.7 s; (b) t=0.9-1.5 s.**

that the liquid can contact the wall surface and continue to vaporize.

Fig. 6 shows the velocity distribution and streamline diagram under the condition of superheat of 80 K. In the initial state, the velocity of the liquid near the wall is small. The fluid flow is disturbed due to the formation and growth of bubbles on the hot-side wall, destroying the velocity boundary layer. The speed of the local area where the bubbles grow increases, eddy currents appear, and the heat transfer ability is strengthened. At time t=1.1 and 1.3 s, due to the existence of bubbles, a low-velocity peak appears near the hot-side. From the streamline diagram, the liquid flows along the wave crest. The existence of the low-velocity peak compresses the upper liquid flow and forms a sudden contraction phenomenon, but increases the velocity of the liquid and increases the disturbance, which is helpful to the heat transfer in the y-direction. However, the overall velocity near the hot-side of the common surface remains low and the near-wall fluid remains inactive.

The simulation results of the superheat degree of 50 K are shown in Fig. 7, Fig. 8 and Fig. 9, respectively, which are the liquid phase distribution, temperature distribution, velocity distribution and streamline diagram at different time. The overall trend of changes over time is not much different from that at 80 K superheat. The difference is that in the gas phase distribution, the number of vaporized cores is reduced to only about 4, and the growth rate of bubbles is also slow. In the temperature distribution, the temperature gradient in the y direction decreases, and the damage degree of the high temperature layer near the hot-side decreases. In the velocity distribution and streamline, the change of the flow velocity near the hot-side is relatively small, the velocity after the bubble detachment becomes smaller, and there are fewer low velocity peaks.

The simulation results with a superheat degree of 20 K are shown in Fig. 10, Fig. 11 and Fig. 12, respectively, which are the gas phase distribution, temperature distribution, velocity distribution and streamline diagram at different times, and the common surface flow with low superheat is basically consistent with the phase transfor-

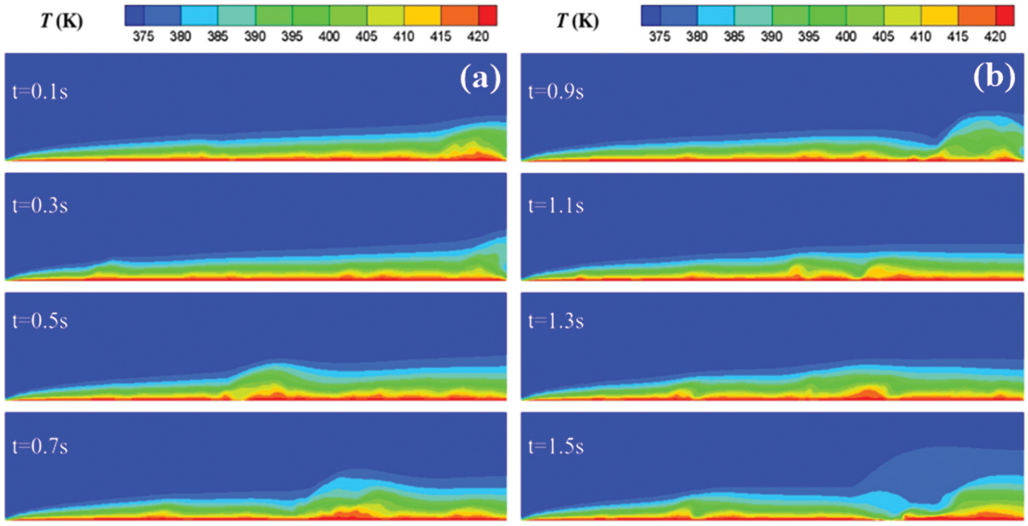



**Fig. 8. Temperature distribution at different time with a superheat of 50 K. (a) t=0.1-0.7 s; (b) t=0.9-1.5 s.**

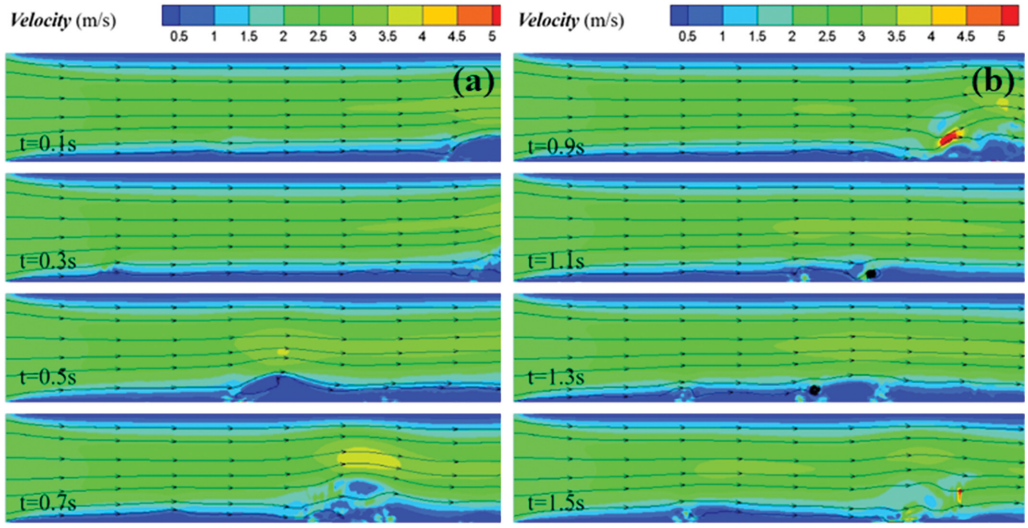



**Fig. 9. Velocity distribution and steam line at different time with a superheat of 50 K. (a) t=0.1-0.7 s; (b) t=0.9-1.5 s.**

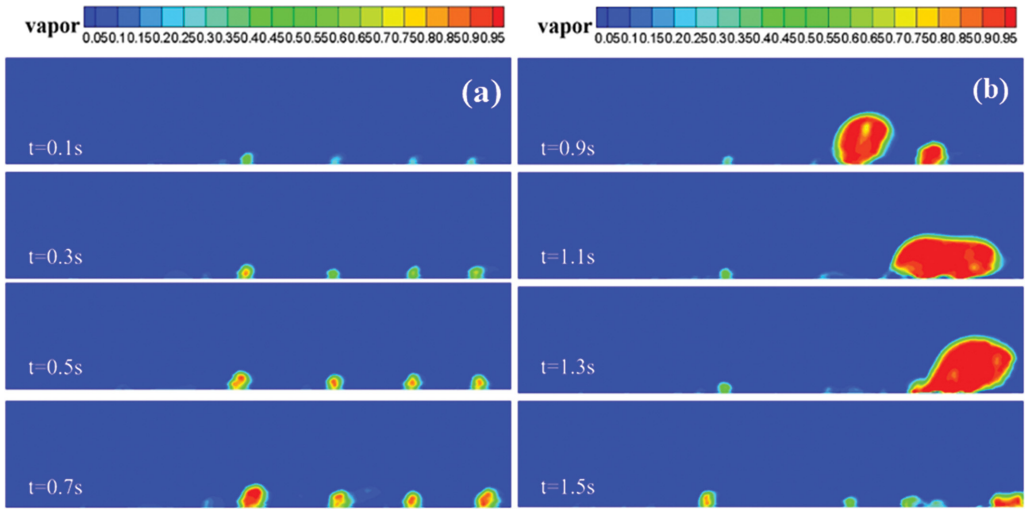



**Fig. 10. Vapor phase distribution at different time with a superheat of 20 K. (a) t=0.1-0.7 s; (b) t=0.9-1.5 s.**

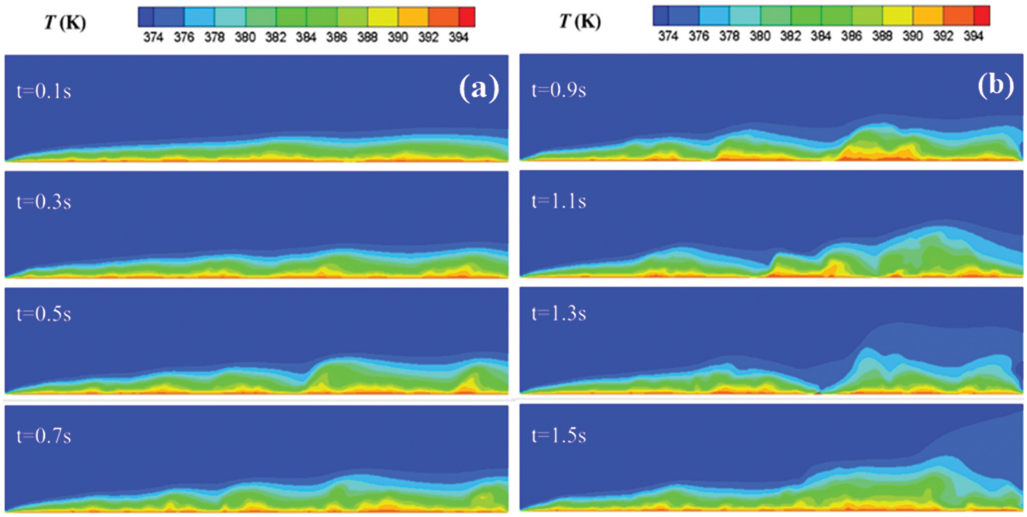



**Fig. 11. Temperature distribution at different time with a superheat of 20 K. (a) t=0.1-0.7 s; (b) t=0.9-1.5 s.**

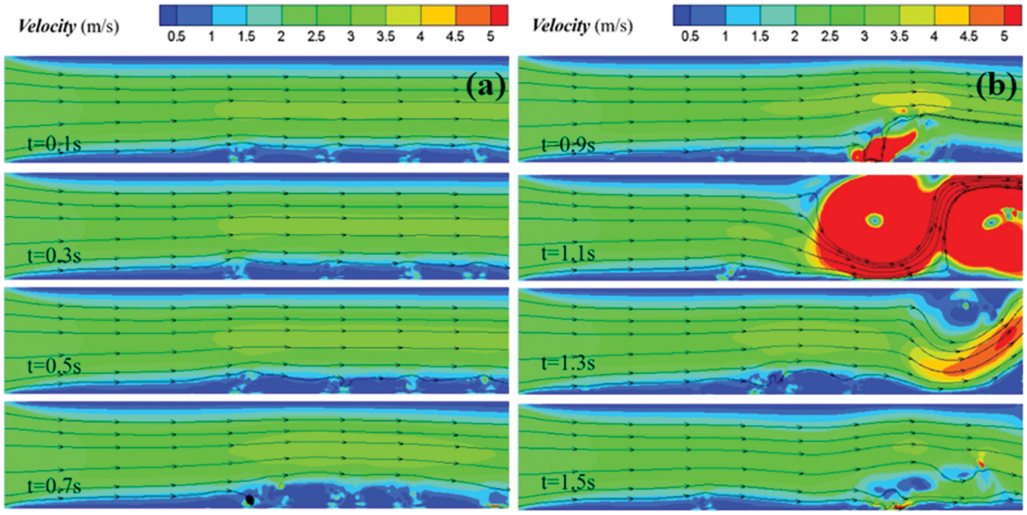



**Fig. 12. Velocity distribution and steam line at different time with a superheat of 20 K. (a) t=0.1-0.7 s; (b) t=0.9-1.5 s.**

mation results. It can be seen from the gas phase distribution that the number of vaporization cores is still about 4. The difference is that at low superheat, the growth of bubbles is slower, and bubble merger does not occur until t=0.9 s. After the liquid flow takes away the generated air bubbles, new air bubbles appear in the original location. It can be seen from the temperature distribution that due to the low superheat degree, the temperature gradient in the y direction is low, and the rise of the high temperature layer caused by the bubble disturbance is also limited, indicating that the heat transfer rate at this time is lower than that of the high superheat degree. Fig. 12 shows the velocity distribution and streamline; it can be observed that the phenomenon of bubble merger is captured at t=1.1 s, the local velocity increases sharply, and the local temperature in this area also increases at this moment. After the bubbles merge, the flow field gradually returns to calm.

**2. Heat Transfer Properties of Superhydrophilic Surfaces**

2-1. L=0 μm

Fig. 13 shows the gas-liquid distribution over time on a superhydrophilic surface with a flower spacing of L=0 μm. It can be seen from that in the early stage of boiling, because the liquid is in a saturated state, after contacting the hot-side, boiling occurs soon and small bubbles appear on the top of the flower and between the flowers. Because the bud structure increases the surface area and the pores between the buds are favorable places for incubating bubbles, the number of vaporized cores on the superhydrophilic surface is significantly higher than that on the common surface. With the passage of time, it can be seen from the front part of the bud at t=0.9-1.5 s, similar to the common surface, the bubbles grow and merge and are separated from the surface under the promotion of the liquid flow and the influence of its own buoyancy, and at the same time, new buds are formed at the original buds for further boiling heat transfer. When the flower spacing is small, the adjacent bubbles are more likely to merge and separate. Due to the wettability of the superhydrophilic surface, the liquid is quickly replenished and continues to boil, so it is not easy to form an air film.

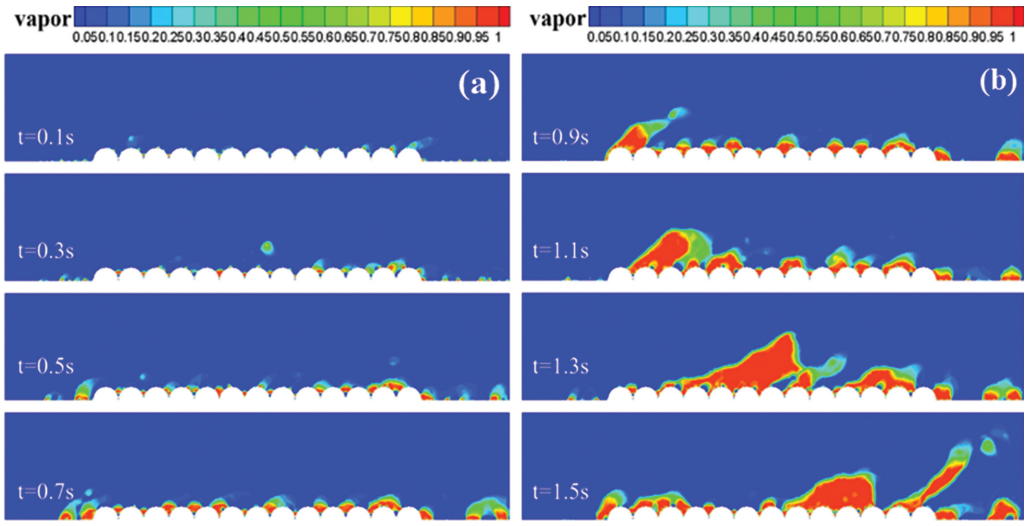



**Fig. 13. Vapor phase distribution of superhydrophilic with L=0 μm at different time. (a) t=0.1-0.7 s; (b) t=0.9-1.5 s.**

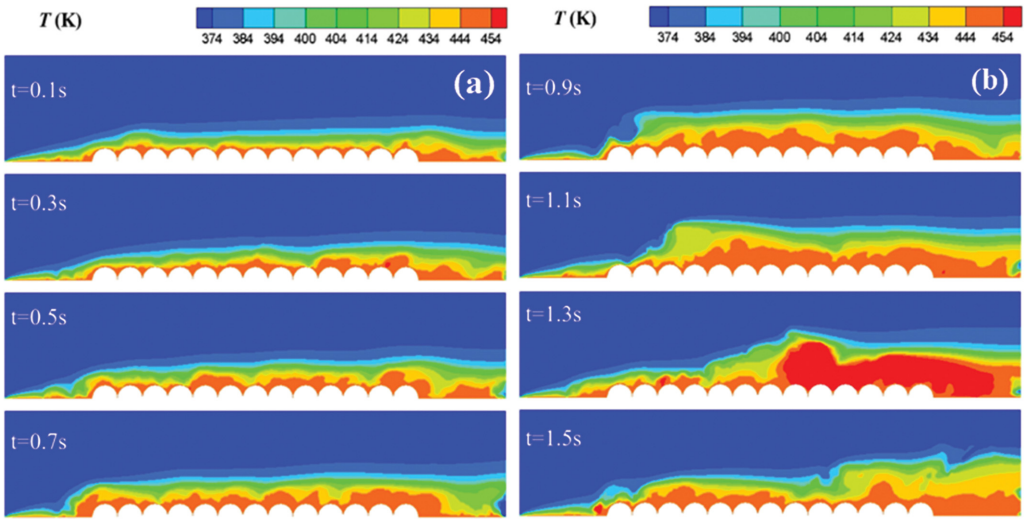



**Fig. 14. Temperature distribution of superhydrophilic with L=0 μm at different time. (a) t=0.1-0.7 s; (b) t=0.9-1.5 s.**

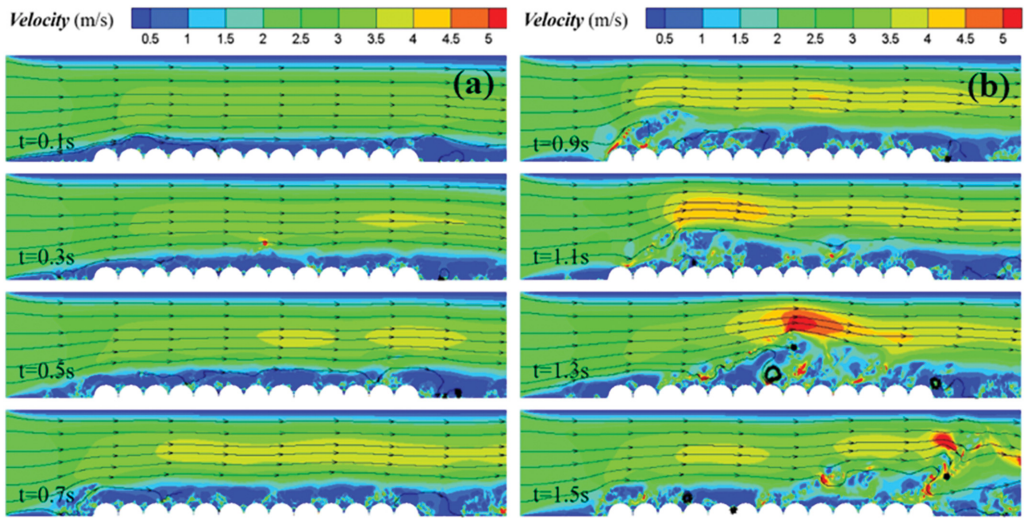



**Fig. 15. Velocity distribution and steam line of superhydrophilic with L=0 μm at different time. (a) t=0.1-0.7 s; (b) t=0.9-1.5 s.**

Fig. 14 shows the temperature distribution of the superhydrophilic surface with L=0 μm. In the initial stage of boiling, the temperature gradient from bottom to top is large and the heat flux is also large, but the high temperature layer is thin. As boiling occurs near the wall of the hot-side, the violent disturbance transfers heat to the liquid, the temperature diffuses upward and the high temperature layer near the wall gradually thickens. With the passage of time, as indicated by t=1.1-1.5 s, the air bubbles at the front buds disengage, new liquid pours in, the high temperature layer near the wall becomes thinner, and the heat is carried away with the air bubbles. Compared with the ordinary surface, the temperature of the fluid on the superhydrophilic surface is higher at the same superheat degree, indicating that the superhydrophilic surface heat transfer is better.

Fig. 15 shows the velocity distribution and streamline diagram of the L=0 μm superhydrophilic surface. The velocity distribution of superhydrophilic surfaces is very complex due to the effect of boiling. In the initial stage of boiling, when t=0.1 s, the vicinity of the wall is a low-velocity region, and with the passage of time the local velocity of the hot-side wall gradually increases. After t=0.5 s, there is a high-speed zone in almost every flower, which is because there are more vaporized cores on the superhydrophilic surface, more bubbles are generated, and high-speed vortices are generated, which in turn disturbs the flow field. From the point of view of bubble detachment at t=0.9-1.5 s, the growing and rising bubbles compress the liquid phase, causing the local velocity to increase, and the velocity from the bubble to the outlet also increases. Compared with the temperature contour in Fig. 14, the temperature at the rear end also rises at this time, indicating that this disturbance is beneficial to heat transfer. Compared with common surfaces, the fluid near the hot-side of the superhydrophilic surface is significantly more active, the area of the low-velocity region is smaller, and the boiling is more intense.

2-2. L=5 μm

The results of the flower spacing L=5 μm are shown in Fig. 16,

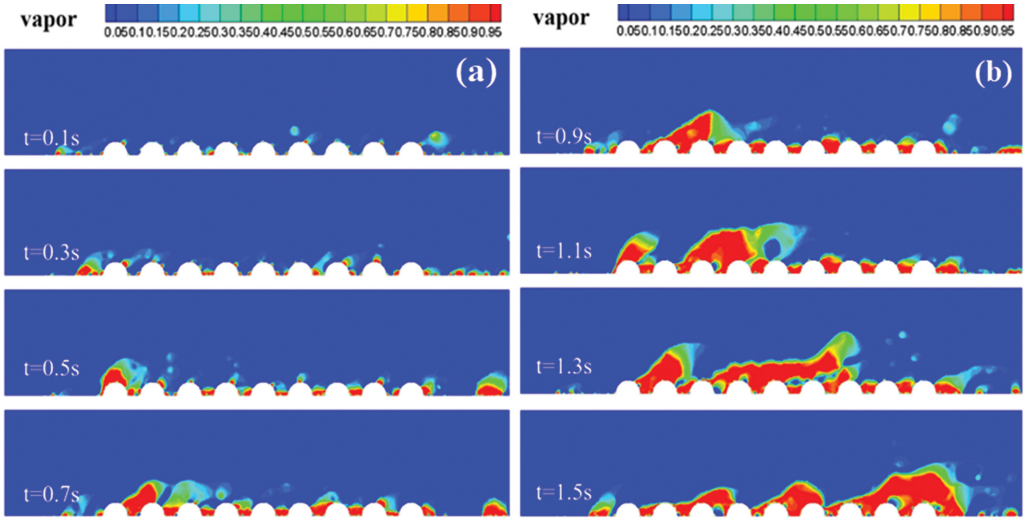



**Fig. 16. Vapor phase distribution of superhydrophilic with L=5 μm at different time. (a) t=0.1-0.7 s; (b) t=0.9-1.5 s.**

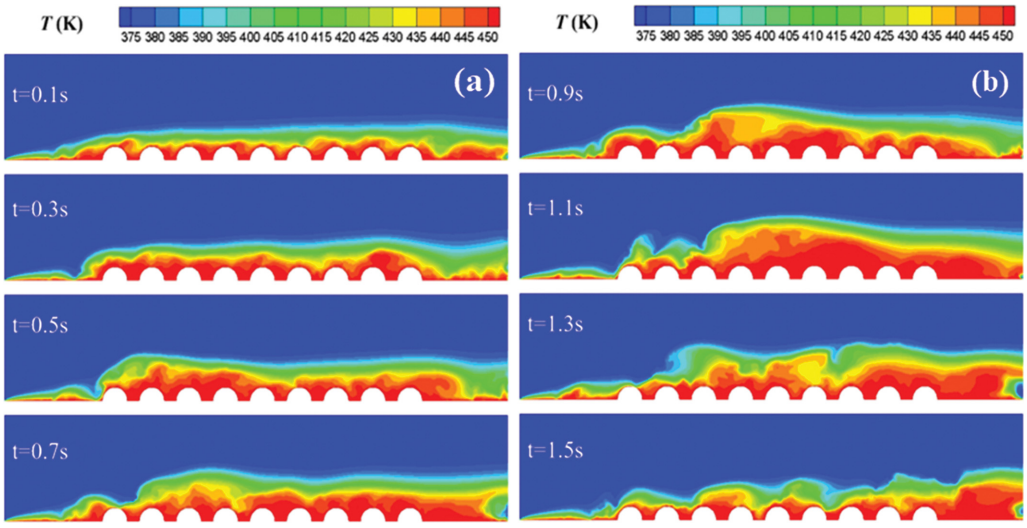



**Fig. 17. Temperature distribution of superhydrophilic with L=5 μm at different time. (a) t=0.1-0.7 s; (b) t=0.9-1.5 s.**

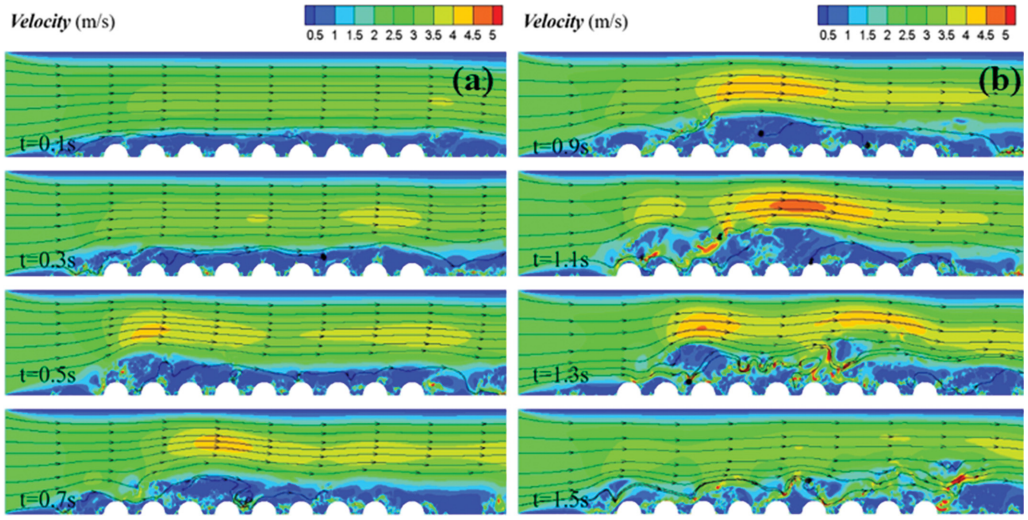



**Fig. 18. Velocity distribution and steam line of superhydrophilic with L=5 μm at different time. (a) t=0.1-0.7 s; (b) t=0.9-1.5 s.**

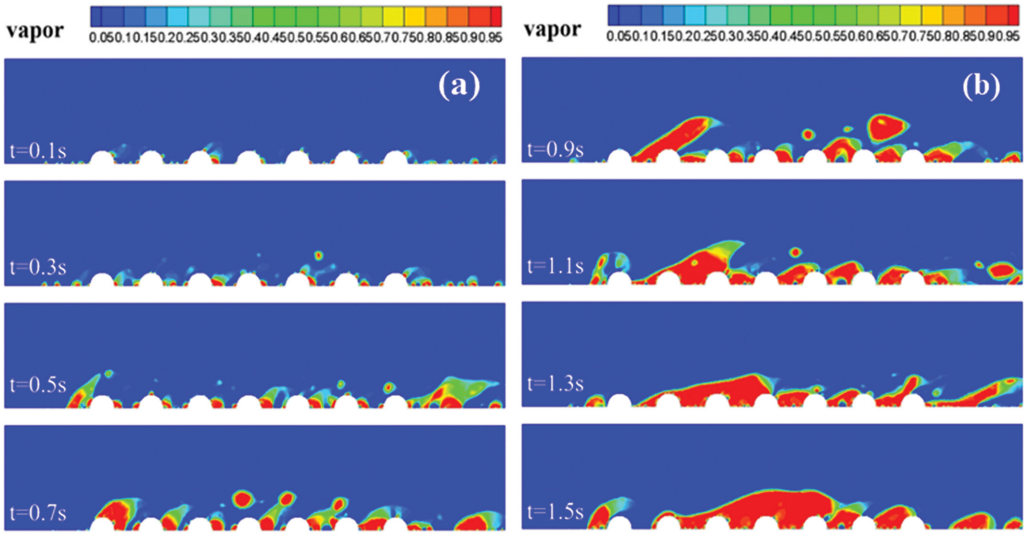



**Fig. 19. Vapor phase distribution of superhydrophilic with L=10 μm at different time. (a) t=0.1-0.7 s; (b) t=0.9-1.5 s.**

Fig. 17 and Fig. 18, respectively, which are the gas phase distribution, temperature distribution, velocity distribution and streamline diagram at different times. Fig. 16 is the gas phase distribution diagram. When the flower spacing increases, the overall trend is similar to the flower spacing L=0 μm. The difference is that the increase of the flower spacing will slightly reduce the heat transfer area, and the number of vaporized cores on the surface will also slightly decrease, mainly in the flower top and the gap between the flowers. The bubbles between the flowers are easy to stick to the wall after growing and merging, and it is difficult to further merge with the adjacent bubbles. Relatively speaking, the bubbles at the top of the flower are easier to break away. At the same time when the large bubbles merge, the resulting fluctuation will cause some small bubbles to detach, and when the large bubbles detach from the hot wall some small bubbles will also be taken away. Compared with common surfaces, superhydrophilic surfaces boil more vigorously and therefore have higher heat transfer capacity.

Fig. 17 shows the temperature distribution of the flower spacing L=5 μm. Over time, the perturbation caused by the growth and merger of bubbles near the hot-side destroys the thermal boundary layer, and the detachment of the bubbles takes away a great deal of heat. At the same superheat, the temperature of the liquid near the superhydrophilic surface will be higher than that of the common surface.

Fig. 18 shows the velocity streamline distribution of the superhydrophilic surface with L=5 μm. Different from the surface of L=0 μm, at the initial stage of boiling (at t=0.3 s), the high-speed zone near the hot-side is mainly concentrated between the flowers and the top of the flowers and the separation is obvious. After t=0.9 s, there are more high-speed areas between the flowers. This is because the growth area of the bubbles is concentrated in the flowers, and the bubbles at the top of the flowers are more easily detached, compressing the liquid flow farther from the hot-side and transferring heat. On the whole, compared with common surfaces, the

velocity boundary layer near the hot-side of the superhydrophilic surface has more obvious damage, and the transition from the low-velocity region to the high-speed region is more natural, which is more helpful for heat transfer.

2-3. L=10 μm

Fig. 19, Fig. 20 and Fig. 21 show the gas phase distribution, temperature distribution, velocity distribution and streamline diagram at different time when the flower spacing L=10 μm.

Fig. 19 shows the vapor phase distribution for the wide flower spacing, which is generally similar to the other two flower spacings. Due to the increase of the flower spacing, the heat transfer area is further reduced, and the number of vaporization cores is also reduced. It can be seen from Fig. 19(a) that in the early stage of growth, the bubbles mainly occur on both sides of the flower bud, and the bubbles on the flower top are easily detached. The bubbles on both sides of the flower grow and eventually merge to fill the gap, making it more difficult for the bubbles to break free. As shown in Fig. 19(b), when the air bubbles in the front flower are detached backwards, they are easily absorbed by the air bubbles in the latter flower, and finally the air bubbles stick to the wall and detach. Although the liquid replenishment can be clearly observed after the bubbles in the front are separated at t=1.5 s, which is beneficial to the heat transfer, the excessively long gas film will have a certain influence on the heat transfer when the bubbles move backwards.

Fig. 20 shows the temperature distribution of the wide flower spacing, but because the spacing is too wide, the bubbles are viscous and the heat transfer capacity is reduced, so the high temperature layer near the wall of the hot-side is relatively thin. Compared with the phase diagram of t=0.9-1.5 s, the viscosity of the bubbles when the bubbles are separated makes the temperature of the rear part show a step shape, so the temperature of the rear part rises. Although the heat transfer is not as good as the narrow flower

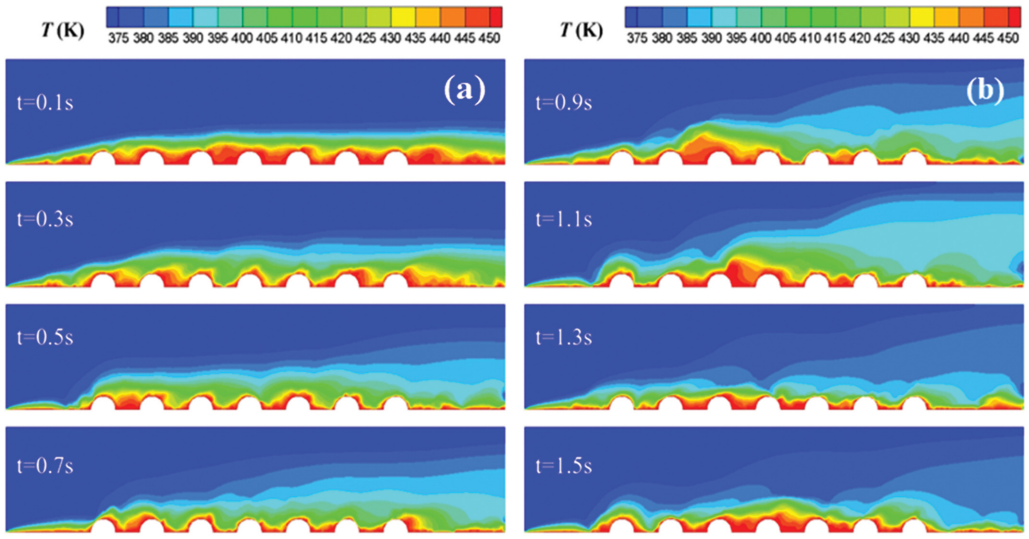



**Fig. 20. Temperature distribution of superhydrophilic with L=10 μm at different time. (a) t=0.1-0.7 s; (b) t=0.9-1.5 s.**

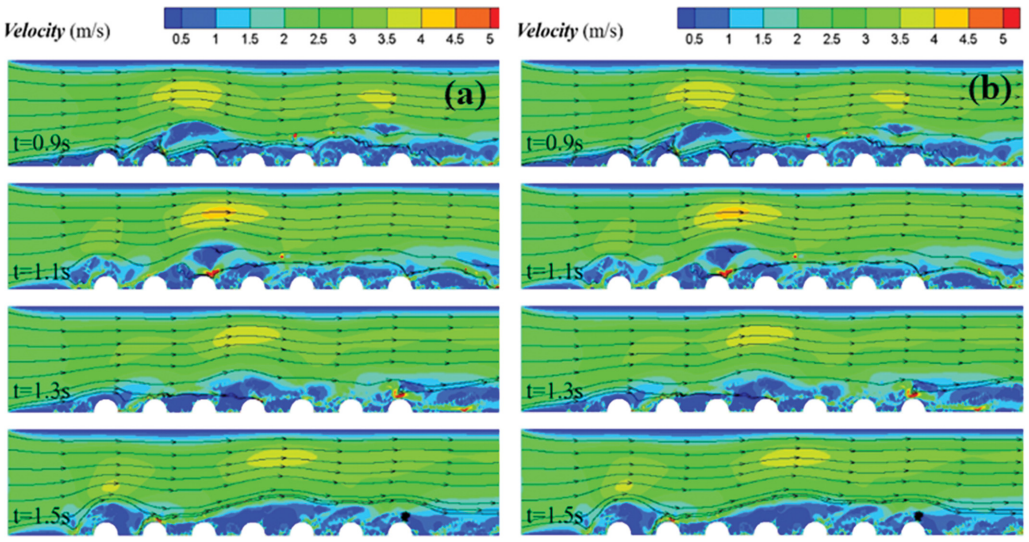



**Fig. 21. Velocity distribution and steam line of superhydrophilic with L=10 μm at different time. (a) t=0.1-0.7 s; (b) t=0.9-1.5 s.**

spacing, under the same superheat degree, the thickness of the high temperature layer near the wall of the hot-side is still larger than that of the common surface, and the heat transfer effect is better.

The velocity and streamline diagrams are shown in Fig. 21. The velocity of the liquid between the flowers is greater at wide flower spacing. Although the overall perturbation is not as good as that of narrow spacing and relatively more low-velocity regions, compared with common surfaces, the superhydrophilic surface with wide floral spacing has more high-speed vortices and more intense surface heat transfer.

### 3. Comparison of Smooth and Superhydrophilic Surfaces

Fig. 22 shows the outlet temperature distribution in the y direction at the equilibrium time. At high superheat, the temperature gradient is significantly larger than that at low superheat. At this time, the heat flux is large and the heat transfer rate is fast. The outlet temperature of L=0 μm is the highest overall, and the outlet temperature of the common surface is the lowest. With the increase of the flower spacing on the superhydrophilic surface, the saturation temperature layer near the adiabatic surface is also larger, but it is still thinner than the common surface. The common surface high temperature layer under low superheat degree is thinner than that of high superheat surface, indicating that the heat carried by the upper liquid phase is limited.

Fig. 23 shows the average outlet temperature, and it can be seen that the average outlet temperature increases for all structural surfaces with increasing superheat. Under the same degree of superheat, the temperature of L=0 μm is the highest, indicating that the boiling takes away the most heat. Compared with the common surface, the superhydrophilic surface with L=0, 5 and 10 μm increases the outlet temperature by up to 4.25%, 2.86% and 2.51%. It shows that the superhydrophilic structure of the surface is helpful to the boiling heat transfer. At the same time, the spacing between the flowers should not be too large, otherwise the heat exchange area and the vaporization core will be reduced.

Fig. 24 measures the heat transfer capacity of the surface by the evaporative heat transfer coefficient. There is a positive correlation between the heat transfer coefficients and superheat degrees of com-

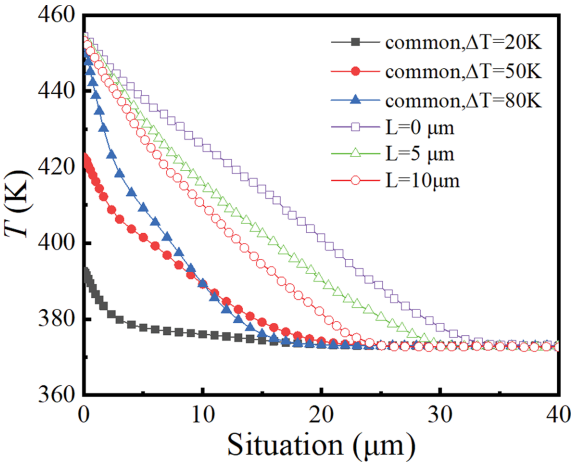



**Fig. 22. Temperature distribution of outlet.**

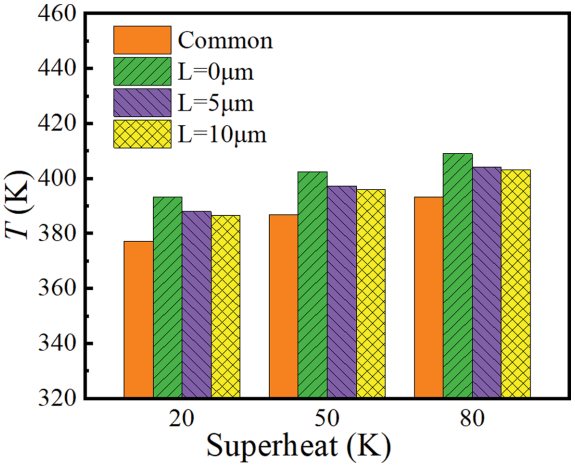



**Fig. 23. Average temperature of outlet.**

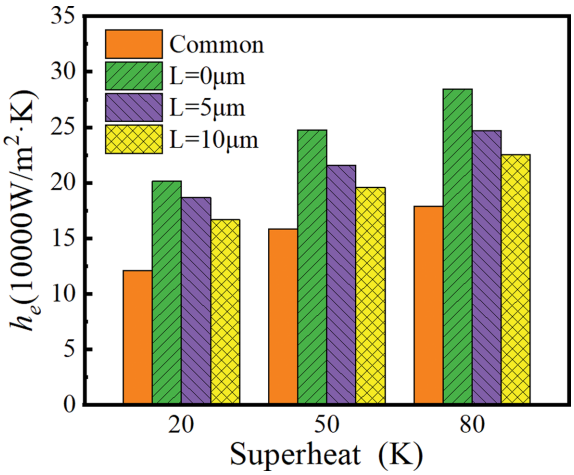



**Fig. 24. Evaporating heat transfer coefficient with different structures and a superheat degrees.**

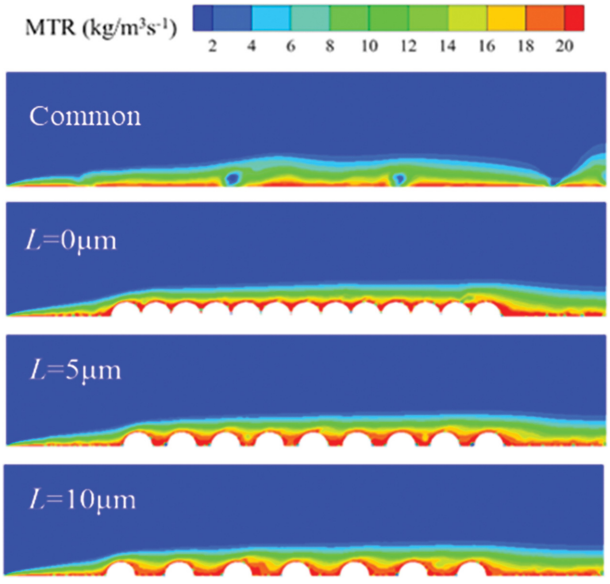



**Fig. 25. Mass transfer rate of surface with different structures.**

mon surfaces and superhydrophilic surfaces. When the superheat degree is 80 K, the heat transfer coefficient of the common surface is 47.5% higher than that of the superheat degree 20 K. It shows that during the nucleate boiling period, the heat flux density increases more. Due to its excellent wettability and bubble inoculation ability, the superhydrophilic surface has the highest heat transfer coefficient when L=0 μm at a superheat of 80 K, which is 1.59 times that of the common surface. At the same time, compared with the similar microcavity surface [47], the bionic flower bud surface has a stronger strengthening effect.

The mass transfer coefficient (MTR, mass transfer rate) of the evaporation surface of different structures under the condition of a superheat of 80 K is shown in Fig. 25. It can be observed that there is a certain relationship between mass exchange and surface area. Relatively speaking, the mass exchange area of superhydrophilic surface is larger, so the overall mass exchange rate is also faster. Due to the untimely replenishment of the liquid phase in some areas of the common surface, the phenomenon of local MTR reduction occurs. Compared with the common surface, the MTR of the superhydrophilic surface with L=0 μm is increased by 23.5%.

## CONCLUSIONS

The boiling conditions of common surfaces and bionic superhydrophilic surfaces with different flower spacings under different superheat degrees were numerically studied, and the gas phase distribution, temperature and velocity distribution contour under different working conditions were obtained. The main conclusions are as follows:

(1) The droplets have more vaporization cores on the superhydrophilic surface, the bubbles can effectively destroy the velocity and temperature boundary layers, and the detached bubbles can compress the upper fluid and increase the flow velocity and temperature behind the bubbles. The heat transfer area is larger under the narrow flower spacing, the vaporization core is more, and the bubble viscosity is smaller.

(2) The outlet temperature of the flower spacing L=0 μm is the highest, which is 4.25% higher than that of the common surface.

(3) The superhydrophilic surface with the flower spacing L=0 μm has the strongest heat transfer capacity at a superheat of 80 K, which is 1.59 times that of the common surface.

(4) Compared with the common surface, the MTR of the superhydrophilic surface with L=0 μm increased by 23.5% when the superheat degree was 80 K.

(5) The bionic flower bud model can effectively improve the effect of boiling heat transfer, which has certain guiding significance for strengthening the boiling end of heat pipes.

## ACKNOWLEDGEMENTS

This work is financially supported by Natural Science Foundation of Jiangsu Province, China (Grant No. BK20181359).

## NOMENCLATURE

A : interface area [$m^2$]
c : specific heat capacity [$J \cdot kg^{-1} \cdot K^{-1}$]
$d_b$ : bubble diameter [m]
E : internal energy [J]
F : surface tension source term [$N \cdot m^{-3}$]
g : acceleration of gravity [$m \cdot s^{-2}$]
h : heat transfer coefficient [$W \cdot m^2 \cdot K^{-1}$]
$h^f$ : standard state enthalpy [$J \cdot kg^{-1} \cdot mol^{-1}$]
$h^s$ : enthalpy of saturated state [$J \cdot kg^{-1} \cdot mol^{-1}$]
k : thermal conductivity [$W \cdot m^{-1} \cdot K^{-1}$]
L : length [m]
$L_{qr}$ : latent heat [$kJ \cdot kg^{-1}$]
$m_{lv}$ : mass exchange rate [$kg \cdot m^{-3} \cdot s^{-1}$]
M : molar mass [$kg \cdot kmol^{-1}$]
P : pressure [Pa]
$R_b$ : bud radius [m]
R : gas constant
S : source term
T : temperature [K]
t : time [s]
u : velocity [$m \cdot s^{-1}$]

### Greek Symbols

$\beta$ : accommodation coefficient
$\eta$ : evaporative heat transfer coefficient
$\mu$ : dynamic viscosity [Pa·s]
$\rho$ : density [$kg \cdot m^{-3}$]

### Subscripts

l : liquid phase
v : gas phase
* : gas phase part

## REFERENCES

1. X. Yang, J. Liu, G. Wang and J. Wei, *Appl. Therm. Eng.*, **210**, 118350 (2022).
2. Y. Wang, C. Qi, R. Zhao and C. Wang, *Appl. Therm. Eng.*, **208**, 118258 (2022).
3. E. C. Okonkwo, I. Wole-Osho, I. W. Almanassra, Y. M. Abdullatif and T. Al-Ansari, *J. Therm. Anal. Calorim.*, **145**(6), 2817 (2021).
4. T. G. Karayiannis and M. M. Mahmoud, *Appl. Therm. Eng.*, **115**, 1372 (2017).
5. Y. Jia, J. Huang, J. Wang and H. Li, *Entropy*, **23**(11), 1482 (2021).
6. Z. Xu, J. Wang, Y. Jia, X. Geng and Z. Liu, *Appl. Therm. Eng.*, **108**, 150 (2016).
7. Y. Jia, S. Yao, J. Wang and H. Li, *Chem. Ind. Eng. Prog.*, **40**(12), 6423 (2021).
8. K. Zhang, L. Bai, H. Jin, G. Lin, G. Yao and D. Wen, *Appl. Therm. Eng.*, **202**, 117759 (2022).
9. S. Rostami, M. Afrand, A. Shahsavar, M. Sheikholeslami, R. Kalbasi, S. Aghakhani, M. S. Shadloo and H. F. Oztop, *Energy*, **211**, 118698 (2020).
10. S. Deb, M. Das, D. C. Das, S. Pal, A. K. Das and R. Das, *Int. J. Heat Mass Transf.*, **170**, 120994 (2021).
11. S. Deb, S. Pal, D. C. Das, M. Das, A. K. Das and R. Das, *Heat Mass Transfer*, **56**(12), 3273 (2020).

12. T. Y. Zhang, L. W. Mou, Y. C. Zhang, J. Y. Zhang, J. Q. Li and L. W. Fan, *Case Stud. Therm. Eng.*, **24**, 100882 (2021).
13. T. Y. Zhang, L. W. Mou and L. W. Fan, *Appl. Therm. Eng.*, **185**, 116453 (2021).
14. A. Recinella and S. G. Kandlikar, *J. Heat Trans-T Asme*, **140**(2), 021502 (2018).
15. K. P. Drummond, D. Back, M. D. Sinanis, D. B. Janes, D. Peroulis, J. A. Weibel and S. V. Garimella, *Int. J. Heat Mass Transf.*, **117**, 319 (2018).
16. P. Cheng, G. Wang and X. Quan, *J. Heat Trans-T Asme*, **131**(4), 043211 (2009).
17. H. Sun, G. Lin, H. Jin, X. Bu, C. Cai, Q. Jia, K. Ma and D. Wen, *Renew. Energ.*, **179**, 1179 (2021).
18. T. P. Rasitha, C. Thinaharan, S. C. Vanithakumari and J. Philip, *Colloid Surf. A*, **636**, 128110 (2022).
19. R. TP and J. Philip, *Appl. Surf. Sci.*, **585**, 152628 (2022).
20. S. C. Vanithakumari, G. Jena, S. Sofia, C. Thinaharan, R. P. George and J. Philip, *Surf. Coat. Tech.*, **400**, 126074 (2020).
21. W. Li, K. Zhou, J. Li, Z. Feng and H. Zhu, *Int. J. Heat Mass Transf.*, **119**, 601 (2018).
22. W. Zhou, D. Han and G. Xia, *Appl. Surf. Sci.*, **591**, 153155 (2022).
23. N. G. Tran and D. M. Chun, *J. Mater. Process. Tech.*, **297**, 117245 (2021).
24. A. S. T. Kaya and U. Cengiz, *Prog. Org. Coat.*, **126**, 75 (2019).
25. T. Adachi, S. S. Latthe, S. W. Gosavi, N. Roy, N. Suzuki, H. Ikari, K. Kato, K. i. Katsumata, K. Nakata, M. Furudate, T. Inoue, T. Kondo, M. Yuasa, A. Fujishima and C. Terashima, *Appl. Surf. Sci.*, **458**, 917 (2018).
26. Y. Ma, J. Tong, M. Zhuang, J. Liu, S. Cheng, X. Pei, H. Li and D. Sang, *Results Phys.*, **15**, 102628 (2019).
27. A. Mahringer, M. Hennemann, T. Clark, T. Bein and D. D. Medina, *Angew. Chem. Int. Ed. Eng.*, **60**(10), 5519 (2021).
28. O. Sato, S. Kubo and Z. Z. Gu, *Accounts Chem. Res.*, **42**(1), 1 (2009).
29. Y. Deng, G. Zhang, R. Bai, S. Shen, X. Zhou and I. Wyman, *J. Membr. Sci.*, **569**, 60 (2019).
30. Y. Feng, F. Chang, Z. Hu, H. Li and J. Zhao, *Int. J. Therm. Sci.*, **163**, 106814 (2021).
31. L. Liao, R. Bao and Z. Liu, *Heat Mass Transfer*, **44**(12), 1447 (2008).
32. R. Liu and Z. Liu, *Int. J. Heat Mass Transf.*, **143**, 118534 (2019).
33. K. Vontas, M. Andredaki, A. Georgoulas, N. Miché and M. Marengo, *Int. J. Heat Mass Transf.*, **172**, 121133 (2021).
34. H. T. Phan, N. Caney, P. Marty, S. Colasson and J. Gavillet, *CR. Mécanique*, **337**(5), 251 (2009).
35. G. D. Sia, M. K. Tan, G. M. Chen and Y. M. Hung, *Case Stud. Therm. Eng.*, **27**, 101283 (2021).
36. G. Yang, J. Liu, X. Cheng, Y. Wang, X. Chu, S. Mukherjee, A. Terzis, A. Schneemann, W. Li, J. Wu and R. A. Fischer, *J. Mater. Chem. A*, **9**(45), 25480 (2021).
37. Y. S. Lim and Y. M. Hung, *Energy Convers. Manage.*, **244**, 114522 (2021).
38. H. Ze, F. Wu, S. Chen and X. Gao, *Adv. Mater. Interfaces*, **7**(14), 2000482 (2020).
39. Y. Nam, E. Aktinol, V. K. Dhir and Y. S. Ju, *Int. J. Heat Mass Transf.*, **54**(7-8), 1572 (2011).
40. C. W. Lin, Y. C. Lin, T. C. Hung, M. C. Lin and H. Y. Hsu, *Int. J. Heat Mass Transf.*, **171**, 121058 (2021).
41. H. Zhan, S. Li, Z. Jin, G. Zhang, L. Wang, Q. Li and Z. Zhang, *J. Mech. Sci. Technol.*, **36**(2), 1025 (2022).
42. K. Ling, Z. Y. Li and W. Q. Tao, *Numer. Heat Tr. A-Appl.*, **65**(10), 949 (2014).
43. K. Vontas, M. Andredaki, A. Georgoulas, N. Miché and M. Marengo, *Int. J. Heat Mass Transf.*, **172**, 121133 (2021).
44. M. Knudesen, *The kinetic theory of gases*, CRC Press. Publications, Boston (1998).
45. D. Lide, *CRC handbook of chemistry and physics*, CRC Press. Publications, Florida (2003).
46. J. Zhang, *Study on enhanced boiling heat transfer characteristics of microstructured heat exchange surfaces*, MA thesis, JUST, Zhenjiang (2016).
47. Y. Lin, Y. Luo, W. Li and W. J. Minkowycz, *Int. J. Heat Mass Transf.*, **179**, 121739 (2021).